Research in Astronomy and Astrophysics, 24:125006 (8pp), 2024 December https://doi.org/10.1088/1674-4527/ad8d1c

Revisit the γ-Ray Flare Associated with Blazar Mrk 421

Xiang-Tao Zeng[1,2,3], Ze-Yuan Tang[1,2,3], and Jun-Hui Fan[1,2,3]
[1] Center for Astrophysics, Guangzhou University, Guangzhou 510006, China; fjh@gzhu.edu.cn
[2] Greater Bay Brand Center of the National Astronomical Data Center, Guangzhou 510006, China
[3] Astronomy Science and Technology Research Laboratory of Department of Education of Guangdong Province, Guangzhou 510006, China
Received 2024 August 24; revised 2024 October 18; accepted 2024 October 28; published 2024 December 3

Abstract

A Very High-energy (VHE) flare was observed by Major Atmospheric Gamma Imaging Cherenkov Telescopes on MJD 57788. This VHE flare was characterized by increased VHE flux and short timescales. In this study, we used one-zone synchrotron self-Compton, two-zone, and spine/layer models to explore this VHE flare's origin. The results indicate that this γ-ray flare can be explained by Inverse Compton Scattering radiation from the layer contributed gamma radiation and results in the γ-ray flare in a different way than the two-zone model. The difference between the two models lies in the performance of spectral energy distribution after γ-ray flare as well as a possible difference in the timescales of the flare.

Key words: radiation mechanisms: non-thermal – (galaxies:) BL Lacertae objects: individual (Mrk 421) – galaxies: jets

1. Introduction

Blazars are a special type of active galactic nucleus, powered by supermassive black holes, with jets directed toward Earth. These jets consist of material moving at high speeds, accelerated to near-light speeds by the magnetic fields of the black hole (Wills et al. 1992; Urry & Padovani 1995).

Blazars are characterized by rapid variability and spectral variability in the full electromagnetic spectrum, additionally core-dominated radio structures. Blazars are also γ-rays sources and some of them are TeV sources. The most extreme properties of blazars can be explained by the beaming effect caused by relativistic jet (Angel & Stockman 1980; Fan et al. 2005; Ghisellini et al. 2014; Fan et al. 2017; Cai et al. 2022; Otero-Santos et al. 2022; Yang et al. 2022b; Zeng et al. 2022; Ouyang et al. 2023).

Blazars can be further divided into two types: BL Lac objects (BL Lacs) and Flat-Spectrum Radio Quasars (FSRQs). The main difference between these two types lies in their spectral line features. BL Lacs (the equivalent width, EW < 5 Å) have very weak or almost non-existent spectral lines, whereas FSRQs (EW > 5 Å) have relatively prominent spectral lines (Stickel et al. 1991).

A typical multiwavelength spectral energy distribution (MWL SED) of a blazar exhibits a distinctive two-bump structure in the $\log\nu - \log\nu F_\nu$ space. In the leptonic model, the low-energy radiation from blazars can be explained as synchrotron radiation from relativistic electrons in the jets, interacting with magnetic fields (Urry 1998). Conversely, the high-energy radiation results from the inverse Compton process (IC; Blumenthal & Gould 1970; Maraschi et al. 1992; Dermer & Schlickeiser 1993; Bloom & Marscher 1996; Błażejowski et al. 2000; Fan et al. 2006) and can be categorized based on the source of the soft photons. These categories typically include: synchrotron self-Compton (SSC; synchrotron emission photons upscattering by the same distribution of electrons) emissions and external Compton (EC; photons arise from external sources outside the jet). The peak frequency of the low-energy peak is known as the synchrotron peak frequency ($\log\nu_p^{\rm syn}$). Fossati et al. (1998) found there is an anti-correlation between the $\log\nu_p^{\rm syn}$ and the synchrotron peak luminosity ($\nu_p^{\rm syn}L(\nu_p^{\rm syn})$). Such an anti-correlation is known as blazar sequence. With a deep understanding on blazar sequences, blazars can be classified based on the synchrotron peak frequency. This classification distinguishes blazars into different types (Nieppola et al. 2006). Abdo et al. (2010) classified blazars into high-synchrotron-peaked blazars (HSPs; $\log\nu_p^{\rm syn} > 15$), intermediate-synchrotron-peaked blazars (ISPs; $14 < \log\nu_p^{\rm syn} < 15$), and low-synchrotron-peaked blazars (LSPs; $\log\nu_p^{\rm syn} < 14$). Further discussions on this topic, supported by a more extensive sample, can be found in the works of Fan et al. (2016) and Yang et al. (2022a).

With the development of ground-based gamma-ray detectors like High Energy Stereoscopic System (Aharonian et al. 2006), Very Energetic Radiation Imaging Telescope Array System (Meagher & VERITAS Collaboration 2015), Major Atmospheric Gamma Imaging Cherenkov Telescopes (MAGIC; Aleksić et al. 2016), The High Altitude Water Cherenkov (Albert et al. 2020) and Large High Altitude Air Shower Observatory (Cao et al. 2024), we are able to have a much clearer view of extragalactic high-energy γ-ray sky. Such great observational data sets provide a good chance to explore the nature of γ-ray emission from blazars (Ghisellini & Tavecchio 2009; Ghisellini et al. 2010, 2014; Chen 2018; Fan et al. 2023).

Mrk 421, a typical and well-studied HSP source, was the first BL Lac object detected in γ-ray band (Lin et al. 1992; Punch et al. 1992). Detailed SED modeling of Mrk 421 is highly beneficial for understanding the high-energy radiation mechanisms of blazars.

Mrk 421 consistently exhibits correlated variability in its X-ray and TeV emissions, along with a similar pattern in its optical and GeV emissions, as reported by various studies (Ahnen et al. 2016; Bartoli et al. 2016; Kapanadze et al. 2016; Sinha et al. 2016). The broadband SED cover from radio to gamma-ray frequencies is effectively modeled using a one-zone SSC model, as demonstrated in previous studies (Cao & Wang 2013; Zheng et al. 2014; Baloković et al. 2016; Zhu et al. 2016; Hu et al. 2023). However, the connection between the variability in each band is still not clear enough. What is more, one-zone model is a phenomenological model. Some special short timescales variability and their related SED are still worth discussing.

MAGIC Collaboration et al. (2021) reported a γ-ray flare associated with Mrk 421 on MJD 57788. A strong Very High-energy (VHE) flux increase characterizes it: the First G-APD Cherenkov Telescope (FACT) observation on the previous day results in a flux of ≈0.4 Crab Nebula flux unit (C. U., Aharonian et al. 2004; Aleksić et al. 2016), while a peak activity of ≈7 C. U. is measured during the outburst. The flux decayed throughout the night with a halving time of approximately one hour. On that night, the averaged flux measured by MAGIC was 3.5 C. U. and the FACT observed 2 C. U. during that night. In this paper, we will investigate the possible origins of this γ-ray flare.

The paper is organized as follows. In Section 2, we briefly describe the one-zone model and the spine/layer model. Section 3 presents the results of SED modeling. The discussion and conclusion are presented in Section 4.

2. Radiative Model

For the two-zone model, we use the same treatment as MAGIC Collaboration et al. (2021) to compare it with the one-zone model.

2.1. One-Zone Model

The calculation of synchrotron and IC emission about the emission region of a homogeneous and isotropic sphere (see the Appendix of Chen 2017 for details).

The spectral power of a relativistic electron traversing in a magnetic field, namely synchrotron emission ($P_{\rm syn}$), can be expressed as

$$P_{\rm syn}(\nu', \gamma) = \frac{2\pi\sqrt{3}e^2\nu_L}{c}\frac{\nu'}{(3/2)\gamma^2\nu_L}\int_{\frac{\nu'}{(3/2)\gamma^2\nu_L}}^{+\infty} K_{5/3}(t)dt, \quad (1)$$

where $K_{5/3}$ is the modified Bessel function of order $5/3$ and $\nu_{\rm L} = eB/2\pi m_e c$ is the Lamer frequency, e is electron charge, m_e is mass of electron, γ is Lorentz factor for electron[4] and ν' stands for frequency in the jet frame.

In the SSC process, the energy density of soft photons, produced by synchrotron emission, is determined by the average energy density ($\bar{U}_{\rm syn}(\nu') = (9/4)L_{\nu'}^{\prime\rm syn}(\nu')/(4\pi R^2 c)$) of these photons within the emission region as in Chen (2017). The SSC spectral power of a single electron can be calculated using the following formula (Blumenthal & Gould 1970; Rybicki & Lightman 1979):

$$P_{\rm ssc}(\nu', \gamma) = 8\pi r_0^2 ch\int f(\gamma, \nu_i, \nu')n_{ph}(\nu_i)d\nu_i, \quad (2)$$

where h is Planck's constant, ν_i is seed photon frequency, $r_0 = e^2/(m_e c^2)$ is classical electron radius and $n_{ph}(\nu_i) = \bar{U}_{\rm syn}(\nu_i)/h\nu_i$ is the seed photon number density. The function $f(\gamma, \nu_i, \nu')$ (The dimensionless Inverse Compton Scattering, ICS spectrum) is given by Blumenthal & Gould (1970)

$$f(\gamma, \nu_i, \nu') = \begin{cases} x[2q\ln q + 1 + q - 2q^2 \\ \quad + \frac{1}{2}\frac{(\Sigma q)^2}{1+\Sigma q}(1-q)\Big] 0 \leqslant q \leqslant 1, \\ 0 \ \text{else} \end{cases} \quad (3)$$

where $x = \nu'/(4\gamma^2\nu_i)$, $q = E/[\Sigma(1+E)]$, $E = h\nu'/(\gamma m_e c^2)$ and $\Sigma = 4\gamma h\nu_i/(m_e c^2)$.

The one-zone model assumes a homogeneous and isotropic emission zone with a uniform electron energy distribution (EED) as described by a broken power-law (BPL):

$$N(\gamma) = N_0\gamma^{-p_1}\left(1 + \frac{\gamma}{\gamma_0}\right)^{(p_1-p_2)}, \quad (4)$$

which can be approximated as:

$$N(\gamma) = \begin{cases} N_0\gamma^{-p_1} & \gamma_{\rm min} \leqslant \gamma \leqslant \gamma_0 \\ N_0\gamma_0^{p_2-p_1}\gamma^{-p_2} & \gamma_0 < \gamma \leqslant \gamma_{\rm max} \end{cases}. \quad (5)$$

N_0 is the normalization constant, p_1 and p_2 are electron energy indexes, γ_0 is broken electron energy, $\gamma_{\rm min}$ and $\gamma_{\rm max}$ is the minimal and maximal energy cut-offs, respectively.

The emission zone with radius R' in the jet frame moves with a Lorentz factor $\Gamma = 1/\sqrt{1-\beta^2}$ (β is the velocity in units of the speed of light, c) and a viewing angle θ. Therefore the bulk motion causes a beaming effect described by the Doppler factor ($\delta = \frac{1}{\Gamma(1-\beta\cos\theta)}$). According to the variability timescale $t_{\rm var}$ and redshift z, one has R equal to $\frac{c\delta t_{\rm var}}{(1+z)}$. The conversion of frequency and luminosity between the jet frame and the AGN frame satisfies the following relationship: $\nu = \delta\nu'$ and $\nu L_\nu = \delta^4\nu' L'_{\nu'}$.

[4] From now on, we will use the term "γ" to represent the electron energy. Since the energy of an electron is $\gamma m_e c^2$, where $m_e c^2$ is the rest energy of the electron.

With the emission power of synchrotron emission and SSC emission, we can calculate the jet frame luminosity $\nu' L'_{\nu} = \nu' \frac{4\pi}{3} R^3 4\pi j(\nu')$, where $j(\nu')$ stands for emitting coefficient is given by (Blumenthal & Gould 1970; Rybicki & Lightman 1979):

$$j_{\rm syn/ssc}(\nu') = \frac{1}{4\pi} \int N(\gamma) P_{\rm syn/ssc}(\nu', \gamma) d\gamma. \quad (6)$$

Observations suggest that the radio emissions from blazars may consist of a combination of multiple optically thick emission regions (Blandford & Königl 1979; Ghisellini et al. 1985); therefore, the self-absorption effect of synchrotron radiation must be taken into account in the SED model. Synchrotron self-absorption coefficient can be calculated as (Rybicki & Lightman 1979):

$$k_{\rm syn}(\nu') = \frac{-1}{8\pi m_{\rm e} \nu'^2} \int \gamma^2 P_{\rm syn}(\nu', \gamma) \frac{d}{d\gamma} \left(\frac{N(\gamma)}{\gamma^2} \right) d\gamma, \quad (7)$$

The optical depth $\tau = k_{\rm syn}(\nu') R$. The total synchrotron luminosity produced by the BPL-EED in this emission zone is given by (Bloom & Marscher 1996; Kataoka et al. 1999):

$$\nu' L'_{\nu}(\nu') = \nu' 2\pi^2 R'^3 j_{\rm syn}(\nu') \frac{2\tau^2 - 1 + (2\tau + 1) e^{-2\tau}}{\tau^3}. \quad (8)$$

At the limit of small τ, one has $\nu' L'_{\nu}(\nu') \simeq \nu' \frac{4}{3} \pi R^3 \cdot 4\pi j_{\rm syn}(\nu') \cdot \left(1 - \frac{3}{4}\tau\right)$.

2.2. The Spine/Layer Jet

Observational evidence indicates that the radio and gamma-ray emissions from blazars are likely produced in different regions, suggesting that the jet is structured (Giroletti et al. 2004; Grandi et al. 2012). Ghisellini et al. (2005) proposed a structured jet model known as the spine/layer model, which describes a two-zone model where a fast inner jet (spine) is surrounded by a larger-scale, slightly slower outer jet (layer). In the spine frame, relativistic electron in the spine can see photons from the layer show strong beaming effects. Similarly, in the layer frame, photons from the spine also show strong beaming effects. The beaming effects in the two frames are determined by the relative velocities of the spine and layer; therefore, the ICS processes of the two-zone will contribute differently to the gamma-ray emission. This model has been widely and successfully used to explain the VHE γ-ray emissions from radio galaxies and blazars (Ghisellini et al. 2005; Tavecchio & Ghisellini 2008; Sikora et al. 2016; Chen 2017; Gaur et al. 2017).

The geometry of the spine/layer model used in this study follows the structure described in Ghisellini et al. (2005). The spine has a radius of R and a width of $\Delta R'_s$ in the comoving frame of the spine. The layer's outer radius is R_2, its width is $\Delta R''_l$ ($''$ refers to values in the frame of the layer, and $'$ refers to values in the frame of the spine). The velocities and corresponding Lorentz factors of the spine and layer are denoted as β_s/Γ_s and β_l/Γ_l, respectively. The relative Lorentz factor between the spine and layer is represented as $\Gamma_{\rm rel} = \Gamma_s \Gamma_l (1 - \beta_s \beta_l)$. Following Chen (2017), the radiation energy densities are considered as follows.

1. In the comoving frame of the layer, the radiation energy density $U''_l = L''_l / [\pi (R_2^2 - R^2) c]$ (slightly different from that of Ghisellini et al. (2005) but following Chen (2017), to make sure that the radiation energy density is in the same format as that in the spine). In the frame of the spine, this radiation energy density will be boosted to $U'_l = \Gamma^2_{\rm rel} U''_l$.
2. In the comoving frame of the spine, the radiation energy within the spine is assumed to be $U'_s = L'_s / [(\pi R^2 c)]$. The radiation energy density observed in the frame of the layer will be boosted by but also diluted (since the layer is larger than the spine) by a factor $\Delta R''_s / \Delta R''_l = (\Delta R'_s / \Gamma_{\rm rel}) / \Delta R''_l$.

3. Results

MAGIC Collaboration et al. (2021) reported a Very High Energy (VHE) flare associated to Mrk 421 observed on Modified Julian Date (MJD) 57788 (2017 February 4). This event is characterized by an approximate tenfold increase in TeV flux on a timescale of just a few hours, with only a slight increase in keV flux. The peak flux in the VHE band is about 7 C. U. during this flare. At lower energy, the UV-optical flux shows no significant variability compared to the day before the flare.

MAGIC Collaboration et al. (2021) published related multi-wavelength data sets. In this paper, we will investigate the possible origins of this VHE flare. To achieve this, we will employ both the one-zone SSC model and the spine/layer model. We plot the evolution of SED under the spine/layer model with the multiwavelength data during the flare (MJD 57786, 57788, 57789) from MAGIC Collaboration et al. (2021).

3.1. Modeling the Multiwavelength SED

3.1.1. One-zone SSC Model

According to MAGIC Collaboration et al. (2021)'s description, this flare occurs in a compact region. Similar to their approach, we limit the radius (R') of the emission zone within $\sim 10^{15}$ cm.

The γ_0 is sensitive to $\nu_p^{\rm syn}$ and $\nu_p^{\rm SSC}$. Combining $\nu_p^{\rm SSC}$ and $\nu_p^{\rm syn}$ allows a very strict limit on γ_0. In the case of Thomson scattering, $\nu_p^{\rm SSC} / \nu_p^{\rm syn} = \frac{4}{3}\gamma_0^2$ while in the case of Klein–Nishina (KN) scattering, $\gamma_0 h \nu'^{\rm syn}_p \gtrsim m_e c^2$. Both cases are useful for limiting γ_0. We did not specifically limit the maximal electron energy $\gamma_{\rm max}$ and make it equal to $100 \times \gamma_0$. For minimum electron energy ($\gamma_{\rm min}$), because of the lack of data in the radio bands, we refer the values from MAGIC Collaboration et al. (2021) in our consideration. The other parameters are presented in Table 1, and the corresponding SED curves are represented by the black line in

Table 1
The Jet Parameters for One-Zone SED Modeling for Mrk 421

Parameters	MAGIC2021		This Work
	Flaring Zone	Quiescent Zone	
δ	25	25	25
$B[10^{-2}\ \mathrm{G}]$	16.5	6.1	6.47
$R[10^{16}\ \mathrm{cm}]$	0.1	1.6	0.64
$N_0[10^3]$	122.1	13.86	4.867
p_1	2	2.3	2.01
p_2	⋯	4	4.04
$\gamma_{\mathrm{min}}[10^3]$	20	1	1.452
$\gamma_0[10^5]$	⋯	1.3	1.713
$\gamma_{\mathrm{max}}[10^6]$	0.6	1.5	17.13

Note. δ: Doppler factor, B: magnetic field strength, R: size of the emission region, N_0: normalized electron number density, p_1: electron energy index, p_2: electron energy index, γ_{min}: minimum electron energy, γ_0: broken electron energy, γ_{max}: maximum electron energy.

Figure 1. In the one-zone model, the TeV band exhibits a very steep tail, whereas the observed TeV spectrum shows a flatter spectrum with a spectral index ∼1.5. This is due to the KN effect, which causes the efficiency of the ICS process to decrease as the photon energy increases, resulting in a steep TeV spectrum.

In proposing a more accurate description of the associated broadband SED, MAGIC Collaboration et al. (2021) advocated for a two-zone leptonic scenario rather than a simple one-zone model. The two zones are labeled as the quiescent zone and the flaring zone. According to this model, the flare's occurrence could be attributed to the emergence of a compact second blob populated by highly energetic electrons characterized by a simple power-law EED. The parameters of this EED are limited by UV-optical flux and the fact that UV-optical flux exhibited a low variability during the observation. It implies that the flaring zone is more energetic than the quiescent zone. The EED of the flaring zone spans a narrow range of electron energy from $\gamma_{\mathrm{min}} = 2 \times 10^4$ to $\gamma_{\mathrm{max}} = 6 \times 10^5$ and its related SEDs are shown as the dashed line in Figure 1. Parameters for quiescent zone were ref from Abdo et al. (2010). A similar two-zone SSC scenario was also employed by Aleksić et al.(2015).

However, it is not clear how such a compact zone could be launched in such a short timescale from the central engine and its related cooling process. The key question is the evolution of such a compact region. If the flaring zone continues to expand, then the light curve should be kept in a high state for some time until it cools down.

But what MAGIC Collaboration et al. (2021) has inspired is that the large increase in VHE luminosity is related to the energy of electrons in the jet and the corresponding ICS process. This suggests a more complex and less homogeneous emitting region. One possible explanation for this complexity involves considering velocity gradients within the jet, as proposed, for example, by Ghisellini et al. (2005).

3.1.2. Spine/Layer Model

Here, we are considering the idea that the production of the SED might be connected to a jet structure with a fast inner spine and a slower outer layer.

The relative motion between the spine and layer results in a certain enhancement in the energy of soft photons during the ICS process in both reference frames. Consequently, this amplification results in distinct (enhanced) IC emissions. This model has been discussed by various studies (Ghisellini et al. 2005; Sikora et al. 2016; Gaur et al. 2017; Wang et al. 2024). What is more, Mrk 421 shows a significant core-jet structure (Lico et al. 2012, 2017).

Chen (2017) explained the hard X-ray excess reported by Kataoka & Stawarz (2016) using the spine/layer model. Chen (2017)'s explanation involves the following scenario: in the spine frame, the EC peak frequency (ν'^{EC}_p) at X-ray (∼3 MeV). This implies that the hard X-ray excess can be produced when synchrotron radiation photons from the layer are scattered by relativistic electrons in the spine. To achieve this hard spectrum in the VHE band, we set ν'^{EC}_p at γ-ray (∼40 GeV) and slightly higher than ν'^{SSC}_p (∼38 GeV).

The spine/layer modeling curves for MJD 57786, 57788 and 57789 are presented in Figure 2 and the related parameters are shown in Table 2. During the flare (MJD 57788), synchrotron radiation and SSC radiation from the spine contribute most of the SED. Similar to the one-zone model, there is a cutoff at higher energy. However, the process of relativistic electrons in the spine scattering photons from the layer contributes to radiation at even higher energy.

4. Discussion and Conclusion

As mentioned in the introduction, the variability of Mrk 421 shows a correlation in certain bands (like X-ray-TeV or optical-Gev). IC processes and the one-zone model can explain such a phenomenon for most situations (Ghisellini & Madau 1996; Ghisellini & Tavecchio 2009; Chen 2017; Hu et al. 2020, 2023). The one-zone model is somewhat less convincing for hard X-ray or shorter timescales TeV variability. The two-zone model will be helpful for some hard TeV spectrums (Aleksić et al. 2015; Xue et al. 2019; Aguilar-Ruiz et al. 2022).

Kataoka & Stawarz (2016) reported hard X-ray excess in HSP BL Lac object Mrk 421 above $\gtrsim$20 keV. Chen (2017) pointed out that this phenomenon could not be the result of the high-energy tail of synchrotron radiation; rather, it was produced by relativistic electrons in the spine scattering synchrotron radiation photons from the layer. Gaur et al. (2017) analyzed X-ray emission (0.6–10 keV) of PKS 2155–304 using the XMM-Newton satellite and the related SED could be easily reproduced in the spine/layer jet structure.

As pointed out in Section 3.1.1, the evolution of the second zone should also influence the light curve. In the next section,

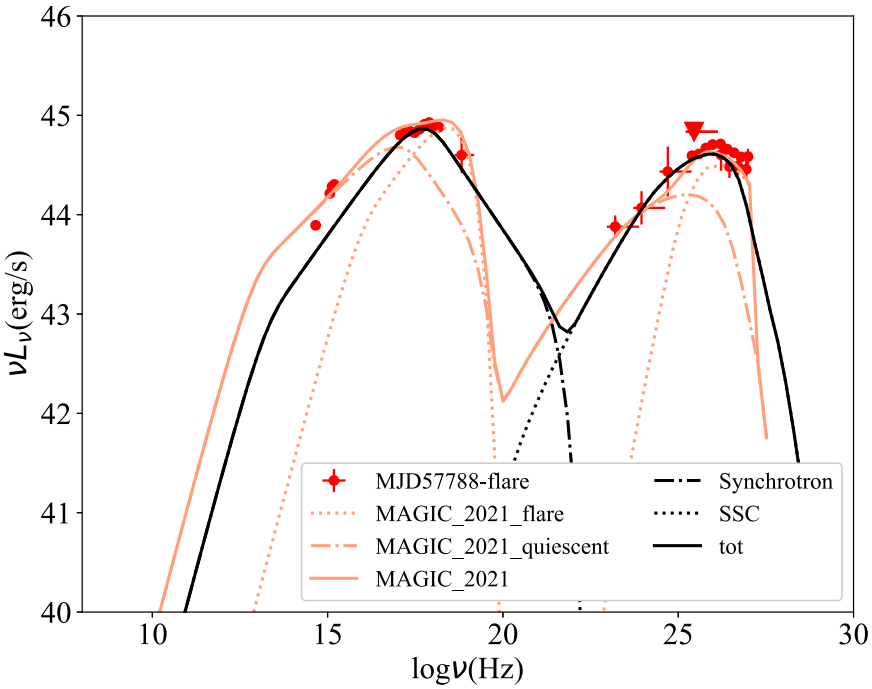

Figure 1. The results of the one-zone synchrotron self-Compton (SSC) SED modeling are presented as follows: the solid black line represents the total radiation, the black dotted–dashed line represents the synchrotron radiation, and the black dotted line represents the SSC radiation. Additionally, the solid orange line represents the results of the two-zone model referred from MAGIC Collaboration et al. (2021), with the orange dotted–dashed line representing the quiescent zone and the orange dotted line representing the flaring zone.

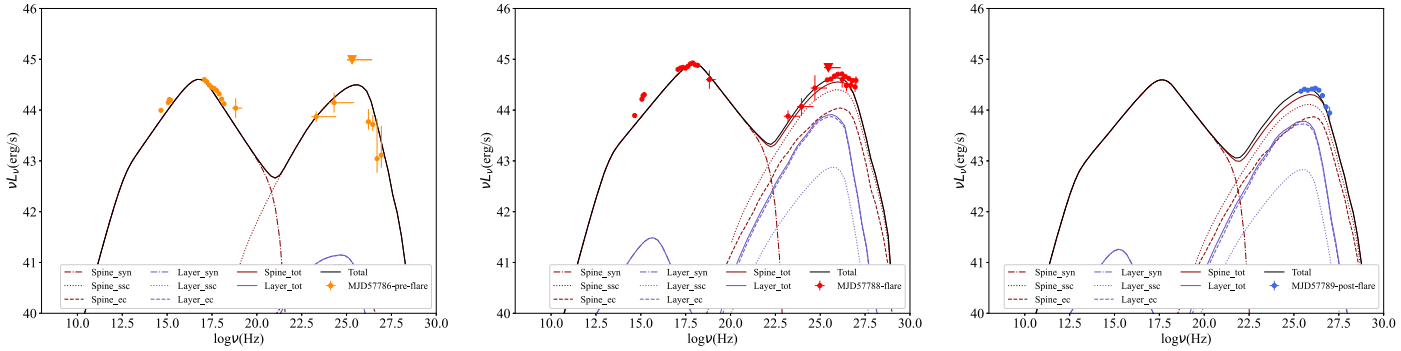

Figure 2. The SED modeling results under the spine/layer model are as follows: The red and blue curves respectively represent the total radiation from spine and layer. The dotted–dashed lines indicate synchrotron radiation, the dotted lines represent SSC radiation, and the dashed lines represent the ICS process with seed photons originating from the layer/spine.

we will discuss the differences between the physical idea in MAGIC Collaboration et al. (2021) and spine/layer jet.

4.1. Explanation under Spine/layer Model

To discuss the differences between the two models, we calculated the jet power ($P_{\rm jet}$, performing a less rigorous calculation, we only calculated the part about electrons) and electron energy density (U_e') using the obtained SED parameters at MJD 57786, 57788 and 57789 and plotted the variation of magnetic field energy density ($U_B' = \frac{B^2}{8\pi}$), γ_0, U_e' and P_{jet} in Figure 3. The U_e' and P_{jet} can be expressed as (Rybicki & Lightman 1979; Ghisellini 2013)

$$U_{\rm e}^{'} = m_{\rm e}c^2 \int \gamma N(\gamma) d\gamma \tag{9}$$

and

$$P_{\rm jet} = \pi R'^2 \Gamma^2 \beta c U_{\rm e}{}'. \tag{10}$$

As mentioned in MAGIC Collaboration et al. (2021), the quiescent zone dominates the SED before the flare. With the

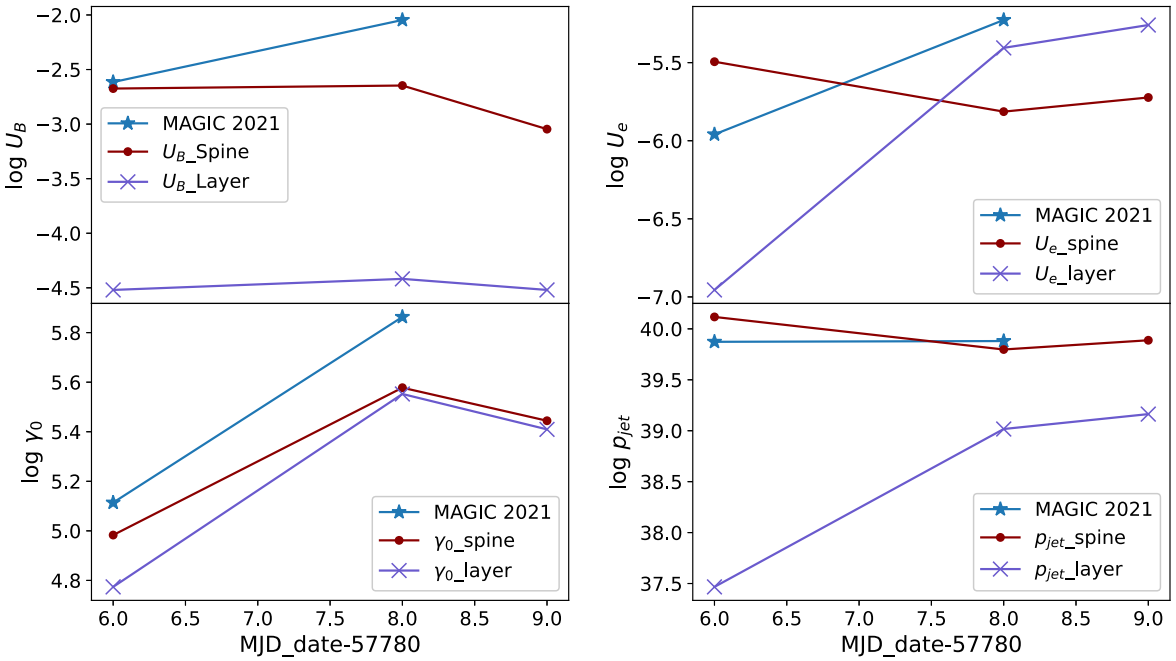

Figure 3. Variation of parameters in log space during the flare. U_B stands for the magnetic field energy density, U_e stands for the electron energy density, γ_0 stands for the broken electron energy, $P_{\rm jet}$ stands for the jet power. The red and blue curves in the figure represent the parameters in the spine and layer, respectively.

Table 2
The Spine/Layer Model Parameters for Mrk 421

MJD Date	Component	Parameters											
		θ (deg)	Γ	δ	B (10^{-2} G)	N_0	$\gamma_{\rm min}$ (10^3)	γ_0 (10^5)	$\gamma_{\rm max}$	p_1	p_2	R (10^{15} cm)	ΔR (10^{15} cm)
57786	Spine	2	22.37	27.79	5.32	2456	0.726	0.9616	$100 \times \gamma_0$	1.98	4.08	9.31	8.85
	Layer	2	4.79	9.23	0.076	853	0.765	0.5941	$100 \times \gamma_0$	2.28	4.7	$1.2 \times R_s$	$30 \times \Delta R_s'$
57788	Spine	2	22.37	27.79	5.67	7880	1.343	3.78	$100 \times \gamma_0$	2.14	3.9	9.31	8.85
	Layer	2	4.79	9.23	0.096	1330	1.202	3.56	$100 \times \gamma_0$	1.82	4.64	$1.2 \times R_s$	$30 \times \Delta R_s'$
57789	Spine	2	22.37	27.79	2.26	6381	1.78	2.28	$100 \times \gamma_0$	2.26	3.66	9.31	8.85
	Layer	2	4.79	9.23	0.076	1867	1.202	2.56	$100 \times \gamma_0$	1.82	4.64	$1.2 \times R_s$	$30 \times \Delta R_s'$

Note. θ: viewing angles. For the geometry parameters, we assume $R_l = 1.2 \times R_s$, $\Delta R_l'' = 30 \times \Delta R_s'$ as Ghisellini et al. (2005) to reduce free parameters.

energy injection from the central engine, a flaring zone was launched. The flaring zone is characterized by a narrower EED with higher energy compared to the quiescent zone, and it dominates the SED during the flare. Due to the data quality and lack of strictly simultaneous MWL data, they do not model the post-flare. Although there are no data for post-flare, we still attempt to model it under the spine/layer based on the idea of cooling down the process of electrons in the spine/layer component.

The spine component behaves in the pre-flare consistent with the quiescent zone (dominates the pre-flare SED). With the energy injection from the central engine, γ_0 and U_B' increase in spine/layer (During this process there may be electrons entering the layer component from the spine component causing the U'_e and $P_{\rm jet}$ of spine component to decrease, this may be related to the dynamics of the spine/layer). The EC emissions of the spine/layer enhanced IC emissions and reproduced the flare. With the cooling of electrons in the spine/layer, the EC emissions will no longer be obvious and the spine component will dominate the SED again.

The following question is whether or not there is a corresponding phenomenon in the observations. Increasingly, radio observations indicate that the radio sources of many TeV sources move at speeds on parsec scales slower than the speeds

theoretically required, while strong TeV emission theoretically necessitates very high speeds to enhance beaming effects (Wardle & Aaron 1997; Edwards & Piner 2002; Mullin & Hardcastle 2009; Weaver et al. 2022). For TeV sources, the jets must be highly relativistic to induce a strong beaming effect that results in extreme observational properties (Cai et al. 2022; Yang et al. 2022b; Ouyang et al. 2023).

According to the unified model, BL Lacs and FR I galaxies (Fanaroff & Riley 1974) should differ only in their viewing angles. However, the number ratio based on viewing angles of BL Lac objects to FR I galaxies estimated by Chiaberge et al. (2000) using a one-zone model is at odds with the observed ratio. Such observational evidence could be considered in two ways: (1) The jet exhibits structural differences and varying speeds; (2) There may be slight differences in viewing angles between the two structures. This is the reason, Ghisellini et al. (2005) proposed that there are transverse structures in AGN jet, characterized by a faster spine and slower layer.

The formation of the spine/layer structure has been explored in various studies. Instabilities in magneto-hydrodynamics (MHD), such as the Kelvin–Helmholtz instability (KHI), are recognized as pivotal factors in the formation of this structure (Lobanov & Zensus 2001; Mizuno et al. 2007; Rossi et al. 2008; Meliani et al. 2010; Yates et al. 2018; Mukherjee et al. 2021; Wang et al. 2023). Such a KHI was used to explain the incidence of intraday variations properties observed in 1ES 2344+514 (TeV blazar, Cai et al. 2022), Cai et al. (2022) estimated critical magnetic field (B_c) and compared it with magnetic field obtained in the one-zone model.

Chand & Böttcher (2024) studied the inverse Compton cooling processes in shear boundary layers (SBLs). They investigated the cooling process of relativistic electrons due to soft photons from outside the jet, which helps improve the spine/layer model to explain certain properties of blazars with rich external photon fields.

In this work, we explore the possible explanation for the γ-ray flare reported by MAGIC Collaboration et al. (2021) under the spine/layer model. The results show that this γ-ray flare can be explained by the interaction of relativistic electrons in the spine/layer with seed photons generated from the layer/spine through IC scattering in a different way than the two-zone model. spine/layer has its advantages in explaining the light curves after the short timescale γ-ray flares. Since in the two-zone model, as the second newly emitted plasma blob expands, the timescale of the γ-ray's flare will not be too short. The key to determining the two-zone with spine/layer is whether the following observation of hard X-ray SED will be characterized by cooling down electrons in the layer component as Chen (2017) described.

We suggested that IC process in different regions and the relativistic effects caused by the relative velocities of the different radiation regions contribute to the hard TeV spectrum observed in TeV blazars. A more detailed theoretical study of the jet structure would greatly help understand the behavior of TeV variability in blazars.

Acknowledgments

We thank Dr. L. Chen for his help in this work. The work is partially supported by the National Natural Science Foundation of China (NSFC, grant Nos. 12433004, U2031201, and 11733001), Guangdong Major Project of Basic and Applied Basic Research (grant No. 2019B030302001). We also acknowledge the science research grants from the China Manned Space Project with No. CMS-CSST-2021-A06, and the support for Astrophysics Key Subjects of Guangdong Province and Guangzhou City. The Key Laboratory for Astronomical Observation and Technology of Guangzhou also supports the work.

References

Abdo, A. A., Ackermann, M., Agudo, I., et al. 2010, ApJ, 716, 30
Aguilar-Ruiz, E., Fraija, N., Galván-Gámez, A., & Benítez, E. 2022, MNRAS, 512, 1557
Aharonian, F., Akhperjanian, A., Beilicke, M., et al. 2004, ApJ, 614, 897
Aharonian, F., Akhperjanian, A. G., Bazer-Bachi, A. R., et al. 2006, A&A, 457, 899
Ahnen, M. L., Ansoldi, S., Antonelli, L. A., et al. 2016, A&A, 593, A91
Albert, A., Alfaro, R., Alvarez, C., et al. 2020, ApJ, 905, 76
Aleksić, J., Ansoldi, S., Antonelli, L. A., et al. 2015, A&A, 578, A22
Aleksić, J., Ansoldi, S., Antonelli, L. A., et al. 2016, APh, 72, 76
Angel, J. R. P., & Stockman, H. S. 1980, ARA&A, 18, 321
Baloković, M., Paneque, D., Madejski, G., et al. 2016, ApJ, 819, 156
Bartoli, B., Bernardini, P., Bi, X. J., et al. 2016, ApJS, 222, 6
Blandford, R. D., & Königl, A. 1979, ApJ, 232, 34
Błażejowski, M., Sikora, M., Moderski, R., & Madejski, G. M. 2000, ApJ, 545, 107
Bloom, S. D., & Marscher, A. P. 1996, ApJ, 461, 657
Blumenthal, G. R., & Gould, R. J. 1970, RvMP, 42, 237
Cai, J., Kurtanidze, S., Liu, Y., et al. 2022, ApJS, 260, 47
Cao, G., & Wang, J. 2013, PASJ, 65, 109
Cao, Z., Aharonian, F., An, Q., et al. 2024, ApJS, 271, 25
Chand, T., & Böttcher, M. 2024, ApJ, 962, 31
Chen, L. 2017, ApJ, 842, 129
Chen, L. 2018, ApJS, 235, 39
Chiaberge, M., Celotti, A., Capetti, A., & Ghisellini, G. 2000, A&A, 358, 104
Dermer, C. D., & Schlickeiser, R. 1993, ApJ, 416, 458
Edwards, P. G., & Piner, B. G. 2002, ApJL, 579, L67
Fan, J., Xiao, H., Yang, W., et al. 2023, ApJS, 268, 23
Fan, J., Yang, J., Xiao, H., et al. 2017, ApJL, 835, L38
Fan, J.-H., Romero, G. E., Wang, Y.-X., & Zhang, J.-S. 2005, ChJAA, 5, 457
Fan, J. H., Yang, J. H., Liu, Y., et al. 2016, ApJS, 226, 20
Fan, Z., Cao, X., & Gu, M. 2006, ApJ, 646, 8
Fanaroff, B. L., & Riley, J. M. 1974, MNRAS, 167, 31P
Fossati, G., Maraschi, L., Celotti, A., Comastri, A., & Ghisellini, G. 1998, MNRAS, 299, 433
Gaur, H., Chen, L., Misra, R., et al. 2017, ApJ, 850, 209
Ghisellini, G. 2013, Radiative Processes in High Energy Astrophysics, Vol. 873 (Berlin: Springer)
Ghisellini, G., & Madau, P. 1996, MNRAS, 280, 67
Ghisellini, G., Maraschi, L., & Treves, A. 1985, A&A, 146, 204
Ghisellini, G., & Tavecchio, F. 2009, MNRAS, 397, 985
Ghisellini, G., Tavecchio, F., & Chiaberge, M. 2005, A&A, 432, 401
Ghisellini, G., Tavecchio, F., Foschini, L., et al. 2010, MNRAS, 402, 497

Ghisellini, G., Tavecchio, F., Maraschi, L., Celotti, A., & Sbarrato, T. 2014, Natur, 515, 376
Giroletti, M., Giovannini, G., Feretti, L., et al. 2004, ApJ, 600, 127
Grandi, P., Torresi, E., & Stanghellini, C. 2012, ApJL, 751, L3
Hu, W., Yan, D., Dai, B., Zeng, W., & Hu, Q. 2020, MNRAS, 493, 410
Hu, W., Yan, D.-H., & Hu, Q.-L. 2023, ApJ, 948, 82
Kapanadze, B., Dorner, D., Vercellone, S., et al. 2016, ApJ, 831, 102
Kataoka, J., Mattox, J. R., Quinn, J., et al. 1999, ApJ, 514, 138
Kataoka, J., & Stawarz, Ł. 2016, ApJ, 827, 55
Lico, R., Giroletti, M., Orienti, M., et al. 2012, A&A, 545, A117
Lico, R., Gómez, J. L., Asada, K., & Fuentes, A. 2017, MNRAS, 469, 1612
Lin, Y. C., Bertsch, D. L., Chiang, J., et al. 1992, ApJL, 401, L61
Lobanov, A. P., & Zensus, J. A. 2001, Sci, 294, 128
MAGIC Collaboration, Acciari, V. A., Ansoldi, S., et al. 2021, A&A, 655, A89
Maraschi, L., Ghisellini, G., & Celotti, A. 1992, ApJL, 397, L5
Meagher, K. & VERITAS Collaboration 2015, in Proc. of the 34th International Cosmic Ray Conference (Trieste: SISSA), 792
Meliani, Z., Sauty, C., Tsinganos, K., Trussoni, E., & Cayatte, V. 2010, A&A, 521, A67
Mizuno, Y., Hardee, P., & Nishikawa, K.-I. 2007, ApJ, 662, 835
Mukherjee, D., Bodo, G., Rossi, P., Mignone, A., & Vaidya, B. 2021, MNRAS, 505, 2267
Mullin, L. M., & Hardcastle, M. J. 2009, MNRAS, 398, 1989
Nieppola, E., Tornikoski, M., & Valtaoja, E. 2006, A&A, 445, 441
Otero-Santos, J., Acosta-Pulido, J., Becerra González, J., et al. 2022, MNRAS, 511, 5611
Ouyang, Z., Xiao, H., Chen, J., et al. 2023, ApJ, 949, 52
Punch, M., Akerlof, C. W., Cawley, M. F., et al. 1992, Natur, 358, 477
Rossi, P., Mignone, A., Bodo, G., Massaglia, S., & Ferrari, A. 2008, A&A, 488, 795
Rybicki, G. B., & Lightman, A. P. 1979, Radiative Processes in Astrophysics (New York: Wiley)
Sikora, M., Rutkowski, M., & Begelman, M. C. 2016, MNRAS, 457, 1352
Sinha, A., Shukla, A., Saha, L., et al. 2016, A&A, 591, A83
Stickel, M., Padovani, P., Urry, C. M., Fried, J. W., & Kuehr, H. 1991, ApJ, 374, 431
Tavecchio, F., & Ghisellini, G. 2008, MNRAS, 385, L98
Urry, C. M. 1998, AdSpR, 21, 89
Urry, C. M., & Padovani, P. 1995, PASP, 107, 803
Wang, J.-S., Reville, B., Mizuno, Y., Rieger, F. M., & Aharonian, F. A. 2023, MNRAS, 519, 1872
Wang, Z.-R., Xue, R., Xiong, D., et al. 2024, ApJS, 271, 10
Wardle, J. F. C., & Aaron, S. E. 1997, MNRAS, 286, 425
Weaver, Z. R., Jorstad, S. G., Marscher, A. P., et al. 2022, ApJS, 260, 12
Wills, B. J., Wills, D., Breger, M., Antonucci, R., & Barvainis, R. 1992, ApJ, 398, 454
Xue, R., Liu, R.-Y., Petropoulou, M., et al. 2019, ApJ, 886, 23
Yang, J. H., Fan, J. H., Liu, Y., et al. 2022a, ApJS, 262, 18
Yang, W. X., Wang, H. G., Liu, Y., et al. 2022b, ApJ, 925, 120
Yates, P. M., Shabala, S. S., & Krause, M. G. H. 2018, MNRAS, 480, 5286
Zeng, X. T., Zhang, Z., Pei, Z. Y., Xiao, H. B., & Fan, J. H. 2022, Ap&SS, 367, 36
Zheng, Y. G., Kang, S. J., & Li, J. 2014, MNRAS, 442, 3166
Zhu, Q., Yan, D., Zhang, P., et al. 2016, MNRAS, 463, 4481